The Astrophysical Journal, 799:75 (8pp), 2015 January 20 doi:10.1088/0004-637X/799/1/75

G305.136+0.068: A MASSIVE AND DENSE COLD CORE IN AN EARLY STAGE OF EVOLUTION

Guido Garay[1], Diego Mardones[1], Yanett Contreras[1,2], Jaime E. Pineda[3], Elise Servajean[1], and Andrés E. Guzmán[1,4]
[1] Departamento de Astronomía, Universidad de Chile, Casilla 36-D, Santiago, Chile
[2] CSIRO Astronomy and Space Science, PO Box 76, Epping NSW 1710, Australia
[3] Institute for Astronomy, ETH Zurich, Wolfgang-Pauli-Strasse 27, 8093 Zurich, Switzerland
[4] Harvard-Smithsonian Center for Astrophysiscs, 60 Garden Street, Cambridge, MA, USA
Received 2014 September 16; accepted 2014 November 14; published 2015 January 16

ABSTRACT

We report molecular line observations, made with ASTE and SEST, and dust continuum observations at 0.87 mm, made with APEX, toward the cold dust core G305.136+0.068. The molecular observations show that the core is isolated and roughly circularly symmetric and imply that it has a mass of $1.1 \times 10^3\ M_\odot$. A simultaneous model fitting of the spectra observed in four transitions of CS, using a non-LTE radiative transfer code, indicates that the core is centrally condensed, with the density decreasing with radius as $r^{-1.8}$, and that the turbulent velocity increases toward the center. The dust observations also indicate that the core is highly centrally condensed and that the average column density is 1.1 g cm^{-2}, a value slightly above the theoretical threshold required for the formation of high-mass stars. A fit to the spectral energy distribution of the emission from the core indicates a dust temperature of 17 ± 2 K, confirming that the core is cold. *Spitzer* images show that the core is seen in silhouette from 3.6 to 24.0 μm and that it is surrounded by an envelope of emission, presumably tracing an externally excited photo-dissociated region. We found two embedded sources within a region of 20″ centered at the peak of the core, one of which is young, has a luminosity of 66 $L_\odot$, and is accreting mass with a high accretion rate of $\sim 1 \times 10^{-4}\ M_\odot$ yr^{-1}. We suggest that this object corresponds to the seed of a high-mass protostar still in the process of formation. The present observations support the hypothesis that G305.136+0.068 is a massive and dense cold core in an early stage of evolution, in which the formation of a high-mass star has just started.

Key words: dust, extinction – ISM: clouds – stars: formation – stars: massive

1. INTRODUCTION

Several single dish surveys of molecular line emission in high density tracers (Plume et al. 1992, 1997; Juvela 1996) and of dust continuum emission (Beuther et al. 2002; Mueller et al. 2002; Faúndez et al. 2004; Williams et al. 2004; Garay et al. 2007) carried out toward luminous sources, either ultra-compact (UC) H II regions and/or luminous IRAS sources, have revealed that young high-mass stars are usually found in massive ($M \sim 10^3\ M_\odot$) and dense (5×10^5 cm^{-3}) cores with sizes of typically ∼0.4 pc and temperatures of typically ∼32 K. Since high-mass stars have already been formed in these cores, which may have appreciably affected their natal environment through stellar winds and radiation, it is not clear whether or not the properties of these cores are representative of the initial conditions necessary for the formation of high-mass stars at the scale of parsecs.

The observational search for massive dense cold cores, capable of forming high-mass stars, but in a stage before star formation begins, started only recently, with the advent of telescopes that allow us to identify them (Garay et al. 2004; Hill et al. 2005; Sridharan et al. 2005; Schuller et al. 2009; Contreras et al. 2013). The bulk of their luminosity is expected to be emitted at millimeter and submillimeter wavelengths. Since high-mass stars are formed in clusters, the determination of the initial conditions of massive star formation is key to understand the formation process that produces a cluster of stars.

In this paper, we report observations of molecular line emission and of continuum emission at 0.87 mm toward G305.136+0.068, a massive dust core identified by Garay et al. (2004) from millimeter observations. The absence of emission in any of the MSX and IRAS bands from this core suggested that it is cold, and therefore a bonafide candidate for being a core in an early stage of evolution. Archival data from the *Spitzer Space Telescope* GLIMPSE survey and from the *Herschel Space Observatory* Hi-GAL project were analyzed to search for embedded sources and to determine the dust temperature of the core, respectively.

2. OBSERVATIONS

2.1. Molecular Lines

The molecular line observations were made using the 10 m Atacama Submillimeter Telescope Experiment (ASTE) located in Pampa La Bola, Chile, and the 15 m Swedish–ESO Submillimetre Telescope (SEST) located on La Silla, Chile. The observed transitions and basic observational parameters are summarized in Table 1.

The ASTE observations were carried out during 2004 December and 2005 July. A detailed description of the characteristics of ASTE is given by Ezawa et al. (2004). The front end consisted of a single pixel heterodyne SiS receiver operating in the 345 GHz band. The back end consisted of four digital autocorrelation spectrometers, each with 1024 spectral channels. The half-power beam width of the telescope at 345 GHz is ∼22″. The main beam efficiency, during night observations, was 0.65. We mapped the CO(3 → 2) and ^{13}CO(3 → 2) emission within a region of 150″ × 150″ in size, with angular spacings of 30″, centered at the peak of the dust core. On-source integration times per map position were one and three minutes for CO(3 → 2) and ^{13}CO(3 → 2), respectively. System temperatures were typically ∼210 K and ∼175 K at the frequencies of the CO(3 → 2) and ^{13}CO(3 → 2) lines, respectively. In addition, we mapped the CS(7 → 6) emission within a region of 60″ × 60″ in size, with 20″ angular spacing. The system temperature was typically ∼370 K and the on-source integration time per map position was

Table 1
Observational Parameters

Line	Frequency (MHz)	Tel.	Beam ($''$)	η_{mb}	Map ($' \times '$)	Spacing ($''$)	Channel width (km s^{-1})	Noise (K)
CS(2 → 1)	97980.968	SEST	52	0.73	4 × 4	30	0.103	0.040
CS(3 → 2)	149969.049	SEST	34	0.66	4 × 4	30	0.087	0.076
CS(5 → 4)	244935.606	SEST	22	0.40	3 × 3	30	0.156	0.123
CS(7 → 6)	342882.950	ASTE	22	0.65	3 × 3	20	0.109	0.094
CO(3 → 2)	345795.990	ASTE	22	0.65	5 × 5	30	0.108	0.090
^{13}CO(3 → 2)	330587.960	ASTE	23	0.65	5 × 5	30	0.113	0.086

four minutes. The data were reduced with the program NEWSTAR and then converted to fits format for further processing with CLASS.

The SEST observations were carried out during 2003 March. We used the high resolution acousto-optical spectrometers, which provided a channel separation of 43 kHz and a total bandwidth of 43 MHz. We mapped the CS(2 → 1) and CS(3 → 2) emission across a region of 2′ in diameter, with angular spacings of 30″, centered at the peak of the dust core. On-source integration times per map position were six and three minutes for the CS(2 → 1) and CS(3 → 2) lines, respectively. The CS(5 → 4) emission was mapped across a region of 1.′5 in diameter, with angular spacing of 30″. On-source integration time per map position was six minutes. System temperatures were typically ∼200 K at 3 mm, ∼290 K at 2 mm and ∼430 K at 1 mm.

2.2. Dust Continuum

The 0.87 mm continuum observations were made using the 12 m Atacama Pathfinder Experiment Telescope (APEX) located at Llano de Chajnantor, Chile. As a receiver, we used the Large Array Bolometer Camera (LABOCA), which is an array made of 295 bolometers arranged in a hexagonal pattern, with two-beam spacing between bolometers (Siringo et al. 2009). The passband of the bolometers has an equivalent width of 60 GHz and is centered at 345 GHz. The HPBW of a single element is 19.″2. The observations were carried out during May of 2008, covering −55° to −60° in longitude, and from −1° to +1° in latitude and are part of the Apex Telescope Large Area Survey of the Galactic Plane (ATLASGAL) survey at 850 μm (Schuller et al. 2009).

Off-line data reduction was performed using the software package, BoA, following the steps described in Siringo et al. (2009). The flux calibration was derived from maps of Uranus. We estimate that the uncertainty in the absolute calibration and pointing accuracy are 20% and 3″, respectively. The noise level achieved in the image is 59 mJy beam^{-1}.

2.3. Ancillary Public Data

In addition to the above observations, we made use of publicly available mid-infrared images taken with the *Spitzer Space Telescope* and far-infrared images taken with the *Herschel Space Observatory*. Mid-infrared images at 3.6, 4.6, 5.8, and 8.0 μm were obtained with the Infrared Array Camera (IRAC; Fazio et al. 2004) as part of the GLIMPSE Legacy Program. Data at 24 μm were obtained with the Multi-band Imaging Photometer as part of the MIPSGAL survey (Carey et al. 2006). The far-infrared images were taken as part of the Herschel Hi-GAL key project (Molinari et al. 2010) using the parallel fast-scanning mode and obtained through the Herschel Science Archive. Images at 70 and 160 μm were obtained using the PACS bolometer (Poglitsch et al. 2010) and images at 250, 350, and 500 μm were obtained using the SPIRE bolometer (Griffin et al. 2010). The two orthogonal scan directions were combined into a single map using the Herschel Interactive Processing Environment (HIPE, v9.2). Cross-scan combination and destriping was performed using the standard HIPE tools over the Hi-GAL maps.

Table 2
Molecular Lines: Observed Parameters[a]

Line	T_A^* (K)	V_{LSR} (km s^{-1})	Δv (FWHM) (km s^{-1})	$\int T_A^* dv$ (K km s^{-1})	θ_d ($''$)
CS(2 → 1)	0.763	−36.41 ± 0.02	4.15 ± 0.04	3.37 ± 0.03	48
CS(3 → 2)	0.378	−36.52 ± 0.02	3.54 ± 0.05	1.42 ± 0.02	38
CS(5 → 4)	0.156	−36.35 ± 0.11	2.59 ± 0.26	0.431 ± 0.04	31
CS(7 → 6)	0.108	−36.48 ± 0.20	5.40 ± 0.64	0.618 ± 0.05	18
CO(3 → 2)	4.79	−36.73 ± 0.01	5.75 ± 0.01	29.3 ± 0.05	64
^{13}CO(3 → 2)	2.06	−36.30 ± 0.01	3.95 ± 0.02	8.66 ± 0.05	59

Note. [a] From Gaussian fits to the spatially averaged emission.

3. RESULTS

3.1. Molecular Lines

Figure 1 shows the CO(3 → 2) and ^{13}CO(3 → 2) spectra observed with ASTE within a 150″×150″ region, centered at the peak position of the dust core. In both transitions, the profiles of the emission from the core ambient gas, centered at −36.5 km s^{-1}, are nearly Gaussian, except in the CO(3 → 2) line at the central position. Toward the whole observed region, the CO(3 → 2) spectra show weak emission at higher velocities than that of the ambient cloud, which most likely arises from foreground or background molecular clouds.

Table 2 gives the observed parameters of the spatially averaged emission in all of the observed transitions. Columns 2–5 give, respectively, the peak antenna temperature, line center velocity, line width, and velocity integrated antenna temperature, determined from a Gaussian fit to the source averaged spectra. The observed line widths are broad, typically ∼4 km s^{-1}, much larger than the thermal width expected for a cloud with $T_K \sim 17$ K, indicating that the G305.136+0.068 core is highly turbulent. At the peak position of the core the CO(3 → 2) and CS(2 → 1) spectra show an excess wing emission, which may indicate the presence of outflowing gas.

Figure 2 presents contour maps of the velocity integrated ambient gas emission in the CO(3 → 2), ^{13}CO(3 → 2), CS(5 → 4), and CS(7 → 6) lines. The range of velocity integration is from −40.9 to −31.1 km s^{-1} for the CO lines and from −40.0 to −33.3 km s^{-1} for the CS transitions. G305.136+0.068 appears as a distinct isolated molecular core. Column 6 of Table 2 gives the FWHM angular size of the core in each observed transition. Assuming that the core is at a

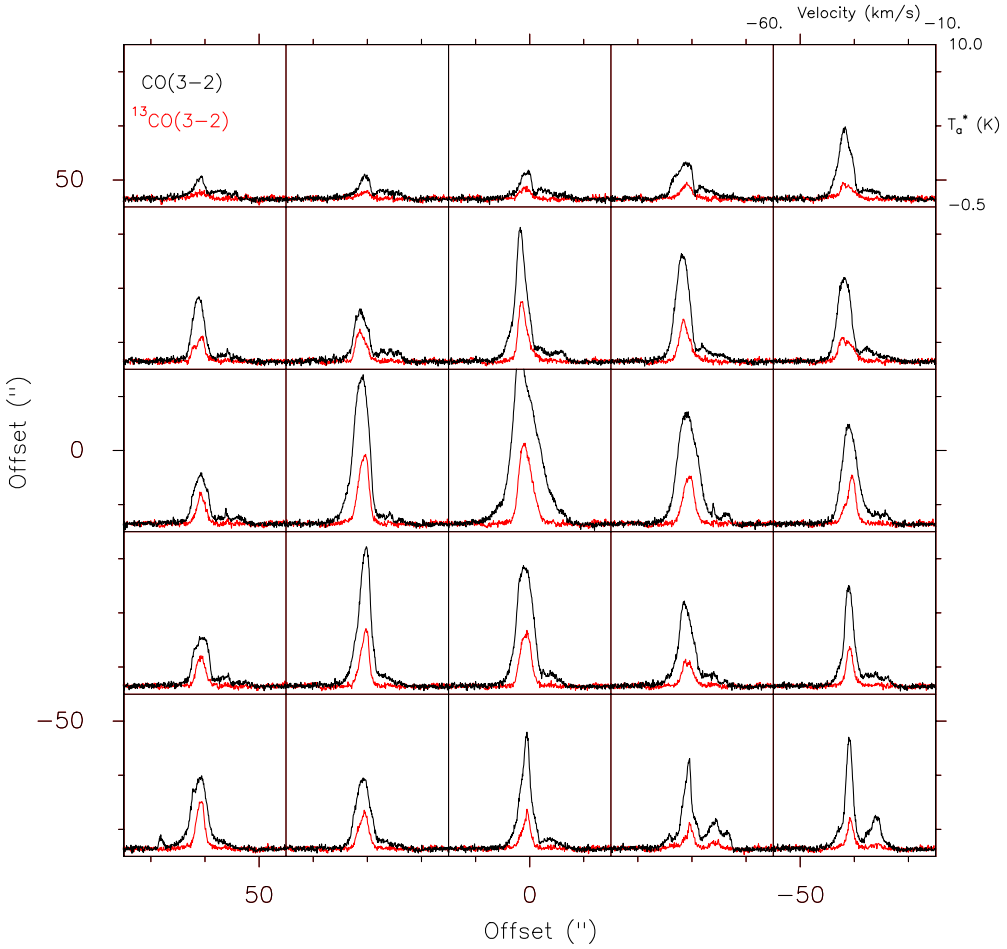

Figure 1. Spectra of the CO(3 → 2) and ^{13}CO(3 → 2) line emission observed with ASTE toward the G305.136+0.068 core. The angular separation between panels is 30″. The velocity scale in each panel runs from −60 to −10 km s^{-1}, and the temperature scale from −0.5 to 10.0 K.

distance of 3.4 kpc (Garay et al. 2004), the radius in the different transitions range from 0.15 to 0.5 pc.

3.2. Dust Emission

Figure 3 presents a contour map of the 0.87 mm continuum emission observed toward the G305.136+0.068 core (upper panel) and, for comparison, a contour map of the 1.2 mm continuum emission (lower panel; Garay et al. 2004). The extent and morphology of the dust continuum emission is similar at both wavelengths. The observed parameters of the cold core at 0.87 mm are given in Table 3. Also given in this table are the parameters of the weak 0.87 mm source located ∼1′.6 SE of G305.136+0.06. Columns 2 and 3 give the peak position. Columns 4 and 5 give, respectively, the peak flux density and the total flux density, and Column 6 gives the deconvolved major and minor FWHM angular sizes determined by fitting a single Gaussian profile to the spatial distribution. We note, however, that Gaussian fits to the spatial distribution of the dust continuum emission do not give good fits.

Figure 4 shows the observed flux density per beam at 0.87 mm as a function of radial distance from the peak position of the core, within a region of 80″ radius. The yellow circles show the average flux at uniformly spaced annuli of 5″ width. A power-law fit to the radial intensity profile, shown by the red curve, does not provide a good fit to the central and outer regions. We find that the observed radial intensity profile, $I(r)$, is best reproduced with the function,

$$I(r) = \frac{I_0}{1 + (r/r_0)^p}, \quad (1)$$

where r is the distance from the center, p is the asymptotic power-law exponent, I_0 is the central intensity, and r_0 is the radius of the central "flat" region. The best fit, shown by the blue curve in Figure 4, gives the following parameters $r_0 = 15''.9 \pm 0''.2$, $I_0 = 3.42 \pm 0.05$ Jy beam^{-1}, and $p = 2.54 \pm 0.03$. If we assume that the temperature and opacity does not change much as a function of radius, then $I(r) \propto N(r)$, where $N(r)$ is the column density, suggesting that the core has a steep density profile. Tafalla et al. (2004), using the same parameterization, found similar density profiles for starless low-mass dense cores.

The mid-infrared GLIMPSE and MIPS images show that the molecular core is seen in silhoutte against the Galactic background emission, indicating that it is cold and that it has opacities greater than one at all wavelengths shorter than 24 μm. Furthermore, in all bands, the core appears to be surrounded by an envelope of emission, with an angular radius of ∼45″. This is illustrated in Figure 5, which presents the 8.0 μm GLIMPSE image toward the G305.136+0.068 core. The envelope is most prominent in the 5.8 and 8.0 μm images and is weak in the 4.5 μm image. The 5.8 and 8.0 μm bands are sensitive to emission from polycyclic aromatic hydrocarbon (PAH) molecules, whereas the 4.5 μm band does not contain any PAH emission features. Thus, the envelope emission is most

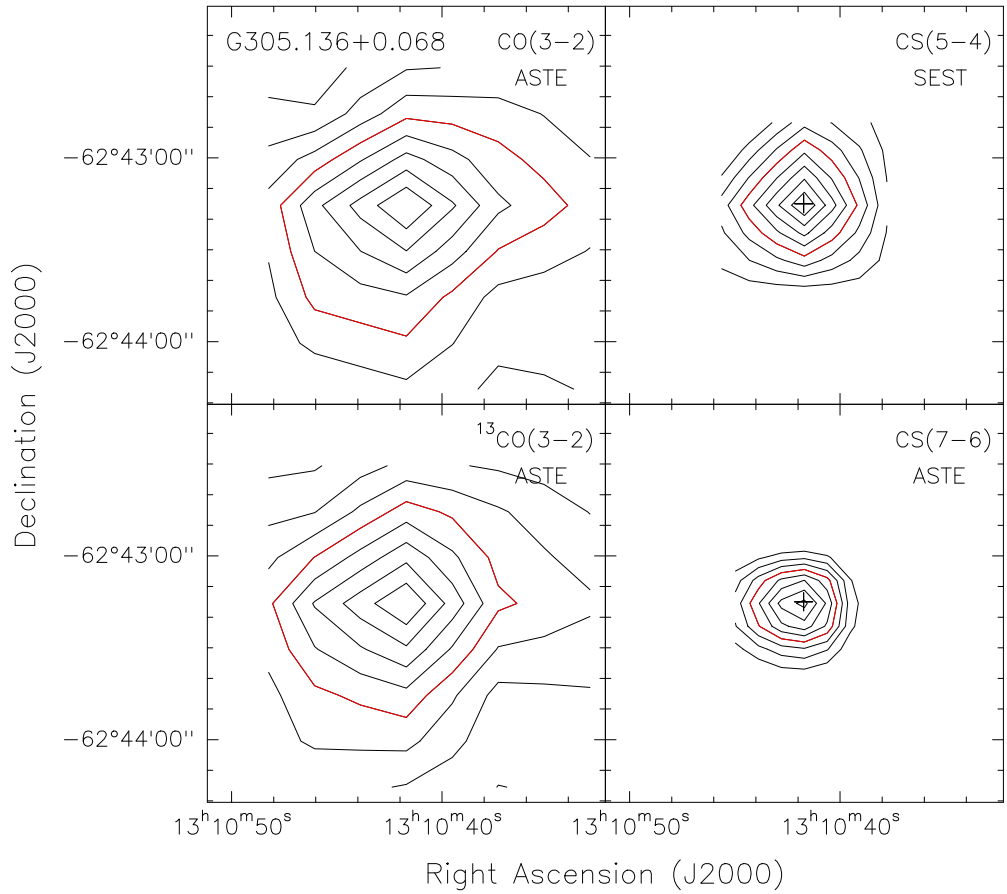

Figure 2. Contour maps of the velocity integrated ambient line emission from the G305.136+0.068 core. Contour levels are drawn at 20%, 30%, 40%, 50%, 60%, 70%, 80%, and 90% of the peak emission. Upper left: CO(3 → 2). Peak emission: 78.5 K km s^{-1}. Lower left: ^{13}CO(3 → 2). Peak emission: 25.0 K km s^{-1}. Upper right: CS(5 → 4). Peak emission: 1.95 K km s^{-1}. Lower right: CS(7 → 6). Peak emission: 2.2 K km s^{-1}. The cross marks the peak position of the dust continuum emission at 1.3 mm (Garay et al. 2004).

Table 3
0.87 MM Continuum Emission: Observed Parameters

Source	Peak Position		Flux Density[a]		Angular Size [b]
	α(2000) h m s	δ(2000) ° ′ ″	Peak (Jy beam^{-1})	Total (Jy)	(″)
G305.136+0.068	13 10 42.06	−62 43 15.6	3.37	16.1	39 × 31
G305.136+0.068SE	13 10 51.97	−62 44 24.2	0.76	3.2	39 × 33

Notes.
[a] Errors in the flux density are dominated by the uncertainties in the flux calibration, of ∼15%.
[b] Errors in the angular sizes are typically 10%.

likely to arise from a photo-dissociated region externally heated by the Galactic UV radiation field.

4. DISCUSSION

4.1. Parameters Derived from Molecular Line Observations

Optical depths, column densities, and total mass of the core were derived from the observations of the CO and ^{13}CO lines as follows. From the ratio of the observed brightness temperatures in the CO and ^{13}CO lines, we derived the opacity in the ^{13}CO line as a function of the velocity in each of the observed positions of the core (see expressions (A2) and (A3) of Bourke et al. 1997). We assumed an excitation temperature of 18 K and a [CO/^{13}CO] abundance ratio of 50.

The total column density of the ^{13}CO molecule in each of the observed positions was then computed from the opacity in the ^{13}CO(3 → 2) line, τ_{13}, and excitation temperature, T_{ex}, using the expression (e.g., Garden et al. 1991)

$$N(^{13}\mathrm{CO}) = 0.81 \times 10^{14} \frac{(T_{\rm ex} + 0.88)\exp(15.87/T_{\rm ex})}{1 - \exp(-15.87/T_{\rm ex})} \times \int \tau_{13} dv \ \mathrm{cm}^{-2}, \quad (2)$$

where v is measured in km s^{-1}. This expression assumes that all energy levels are populated according to local thermodynamic equilibrium at the temperature $T_{\rm ex}$. We find that the ^{13}CO column density at the peak position of the core is 2.0 × 10^{16} cm^{-2}. Integrating the column densities over the solid angle subtended

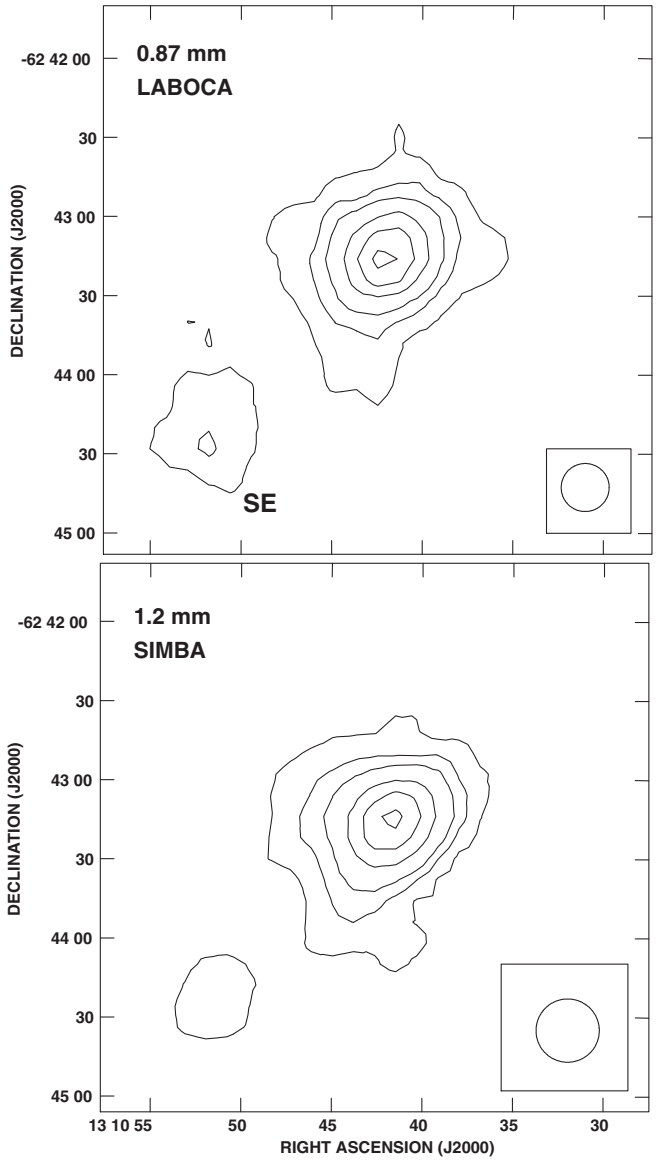

Figure 3. Maps of dust continuum emission observed toward G305.136 + 0.068. The FWHM beam is shown at the bottom right. Top: 0.87 mm emission. Contour levels are drawn at 1, 2, 3, 5, 7, and 9 × 0.35 Jy beam^{-1}. The 1σ rms noise is 59 mJy beam^{-1}. Bottom: 1.2 mm emission. Contour levels are drawn at 1, 2, 3, 5, 7, and 9 × 0.15 Jy beam^{-1}. The 1σ rms noise is 36 mJy beam^{-1}.

by the core and assuming a [H_2/^{13}CO] abundance ratio of 5×10^5 (Pineda et al. 2008), we derive that the core has a total mass of $1.1 \times 10^3\ M_\odot$. The molecular density derived from this mass and the observed radius in the ^{13}CO line, of 0.49 pc, assuming that the core has uniform density, is $\sim 4 \times 10^4$ cm^{-3}.

Another estimate of the total mass using the molecular line observations can be made assuming that the core is in virial equilibrium (MacLaren et al. 1988). From the observed size and average line width in the ^{13}CO(3 → 2) and CS(2 → 1) transitions, we derive virial masses of 1.4×10^3 and $1.2 \times 10^3\ M_\odot$, respectively.

4.2. Parameters Derived from Dust Observations

The parameters of the core derived from the 0.87 mm observations are summarized in Table 4. To determine the core dust temperature, we made use of the publicly available Herschel images in the wavelength range from 70 to 500 μm. Figure 6 shows the spectral energy distribution (SED) from 70 μm to 1.2 mm. In this wavelength range, the emission is mainly due to thermal dust emission. The flux density at 70 μm corresponds to an upper limit. We fitted the SED using a modified blackbody

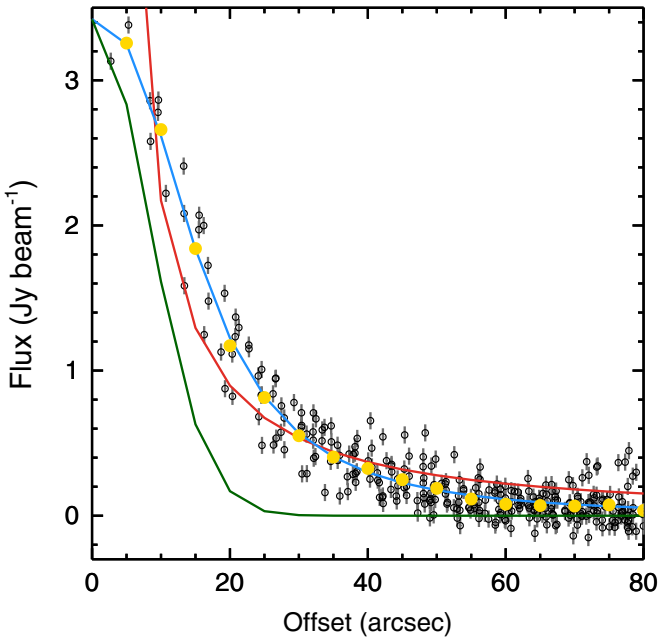

Figure 4. Radial intensity profile of the 0.87 mm continuum emission toward the G305.136+0.068 core. The blue and red lines correspond, respectively, to a fit of the observed radial intensity with the function given in Equation (1) and a power-law fit. The yellow circles show the average flux at different annuli. The green line corresponds to the beam response of the telescope at 0.87 mm (Siringo et al. 2009).

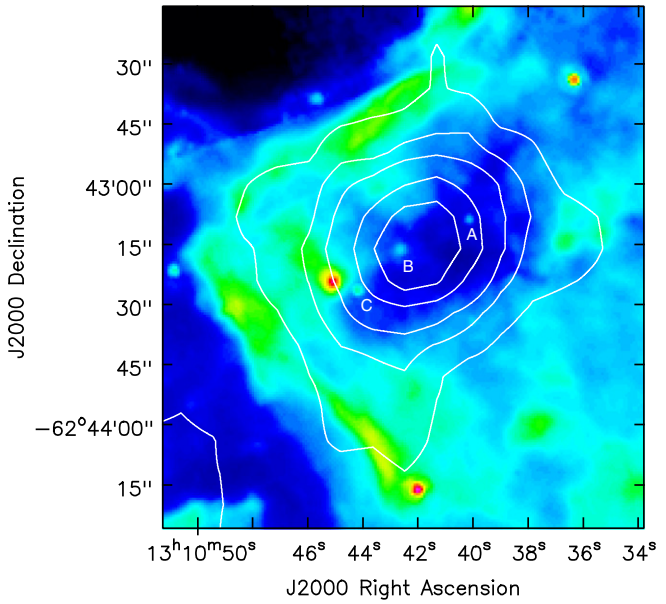

Figure 5. 8.0 μm GLIMPSE image of the G305.136+0.068 core overlaid with contours of the 0.87 mm emission. Labeled are compact sources projected toward the dust core.

Table 4
Dust Emission: Derived Parameters

Source	T_d (K)	Radius (pc)	Mass ($M_\odot$)	n(H_2) (cm^{-3})	N(H_2) (cm^{-2})	$\tau_{0.87\,mm}$
G305.136+0.068	17.	0.29	1.2×10^3	2.0×10^5	2.4×10^{23}	0.02

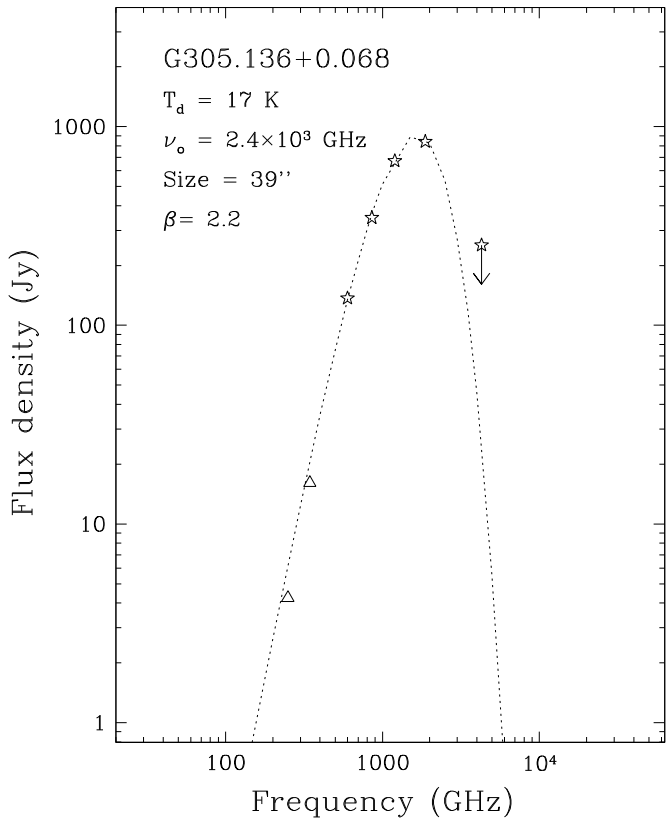

Figure 6. Spectral energy distribution of the G305.136 + 0.068 core. The dotted line indicates the best fit with a single temperature modified black body model. Listed are the fitted parameters.

function of the form $B_\nu(T_d)[1 - \exp(-\tau_\nu)]\Omega_s$, where τ_ν is the dust optical depth, $B_\nu(T_d)$ is the Planck function at the dust temperature T_d, and Ω_s is the solid angle subtended by the dust emitting region. The opacity was assumed to vary with frequency as ν^β, i.e., $\tau_\nu = (\nu/\nu_o)^\beta$, where ν_o is the frequency at which the optical depth is unity, referred to as the turnover frequency. The best fit to the SED, shown as the dotted line in Figure 6, indicates a dust temperature of 17 K, a turnover frequency of 2.4×10^3 GHz, an angular size of 39″, and a dust opacity power-law index of 2.2. The column density derived from the turnover frequency is 2.6×10^{23} cm^{-2}. This value, equivalent to 1.1 g cm^{-2}, is slightly above the theoretical threshold required for the formation of high-mass stars (Krumholz & McKee 2008), suggesting that the G305.136+0.068 core will form high-mass stars.

Assuming that the observed flux density at 0.87 mm, $S_{0.87\mathrm{mm}}$, corresponds to optically thin, isothermal dust emission, then the mass of the core, given in Column 4 of Table 4, was determined using the expression (e.g., Chini et al. 1987),

$$M_g = \frac{S_{0.87\,\mathrm{mm}} D^2}{R_{dg} \kappa_{0.87\,\mathrm{mm}} B_{0.87\,\mathrm{mm}}(T_d)}, \quad (3)$$

where R_{dg} is the dust-to-gas mass ratio (assuming 10% He) with a value of 0.01, $\kappa_{0.87\,\mathrm{mm}}$ is the mass absorption coefficient of dust with a value of 2 cm^2 g^{-1} (Ossenkopf & Henning 1994), and $B(T_d)$ is the Planck function at the dust temperature T_d. The mass derived is $1.2 \times 10^3\ M_\odot$, in good agreement with the LTE mass and the virial masses. The average molecular density and average column density, derived from the mass and radius, assuming that the core has uniform density, are given in Columns 5 and 6 of Table 4. We stress that these values should be taken with caution, since, as discussed in Section 3.2, the G305.136 + 0.068 cold core exhibits a steep density gradient. Finally, Column 7 of Table 4 gives the average continuum optical depth at 0.87 mm. It takes a value of 0.02, consistent with the optically thin assumption.

The similar values of the molecular gas mass (derived from both the dust continuum emission and LTE analysis) and the virial mass (which measures the gas plus stellar mass), suggest that a significant fraction of the total mass of this massive dense cold core is in the form of molecular gas, and hence that the gas dominates the gravitational potential.

4.3. Parameters Derived from Line Profile Modeling

As previously discussed, the physical conditions in the core are unlikely to be uniform, but depend on the distance from the central region. To determine the physical structure of the cloud, model profiles in the CS $J = 2 \rightarrow 1$, $3 \rightarrow 2$, $5 \rightarrow 4$, and $7 \rightarrow 6$ lines were computed and compared with the observed profiles. The model profiles were obtained using a Monte Carlo radiative transfer code (Mardones 1998) based on Bernes (1979). To obtain a reliable CS ($7 \rightarrow 6$) profile, we used 14 levels and 13 transitions in the Monte Carlo simulation. The robustness of the Monte Carlo method is widely discussed by van Zadelhoff et al. (2002).

To model a cloud requires us to adopt the dependencies of the physical parameters with radius. Here we assume that the density, kinetic temperature, velocity field, and turbulent velocity follow power-law dependencies with radius. Besides the great simplicity and flexibility in the program provided by this choice, these are realistic assumptions. We find that the simple power-law model can fit the observed data very well. This is illustrated in Figure 7, which shows the four CS spectra observed at the peak position of the core and the results of the best fit model (dotted line). We assumed a [CS/H_2] abundance ratio of 2.2×10^{-10} (Tafalla et al. 2004). The model fit implies that the core is very dense and highly centrally condensed, with the density depending with radius as

$$n = 1.6 \times 10^5 \left(\frac{r}{0.3\,\mathrm{pc}}\right)^{-1.8} \mathrm{cm}^{-3},$$

with minimum and maximum radius of 0.01 and 1 pc, respectively. The model fit also indicates that the turbulent velocity increases toward the center of the core as

$$V_{\mathrm{turb}} = 1.4 \left(\frac{r}{0.3\,\mathrm{pc}}\right)^{-0.2} \mathrm{km\ s}^{-1}.$$

This result is supported by recent observations which show that the line width increases toward the center (Servajean et al. 2014, private communication). Finally, the model fit also implies that the core is cold, and that the temperature slightly increases toward the center as

$$T_K = 16 \left(\frac{r}{0.3\,\mathrm{pc}}\right)^{-0.15} \mathrm{K}.$$

4.4. Embedded Sources

We searched for embedded sources within the core by inspecting all images available to the public taken with the *Spitzer* telescope. Within a region of 20″ in radius, centered at the peak position of the dust core, we identified three compact

Table 5
Embedded *Spitzer* Sources

Source	R.A.(J2000)	Decl.(J2000)	Flux Density (mJy)				
			3.6 μm	4.5 μm	5.8 μm	8.0 μm	24.0 μm
A	13 10 40.212	−62 43 9.03	0.8673	4.219	9.852	13.91	21.515
B	13 10 42.713	−62 43 16.52	... [a]	14.56	21.18	18.45	95.281
C	13 10 44.158	−62 43 26.46	11.52	20.12	27.05	29.12	... [b]

Notes.
[a] Not given.
[b] Projected toward a strong background extended emission.

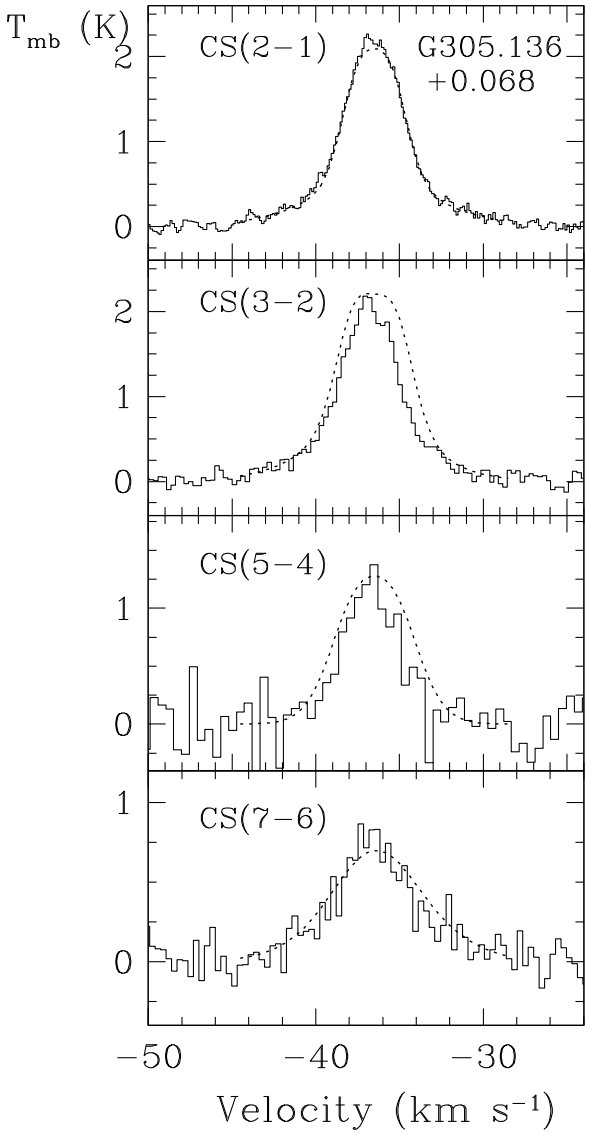

Figure 7. Monte-Carlo simulation of the CS transitions. Continuous lines correspond to the observed spectra and dotted lines to the simulated spectra.

sources that appear in both the 8 μm and the 24 μm images, making them good candidates for embedded objects. These sources, labeled A, B, and C in Figure 5, were also detected in all of the other IRAC bands. The observed parameters of the three objects are given in Table 5. Columns 2 and 3 give the coordinates, Columns 4–8 the flux densities measured at 3.6, 4.6, 5.8, 8.0, and 24 μm, respectively.

The spectral energy distributions of these objects were analyzed by fitting model SEDs using a large grid of precomputed models (Robitaille et al. 2007). The SED fitting indicates that two of the three sources (A and B) correspond to embedded objects. Source B, which is located closest to the peak position of the dust core, is most likely a very young protostellar object (age of 6×10^4 yr) with a mass of 2.6 $M_\odot$, a luminosity of 66 $L_\odot$, and associated with an envelope accreting at a high rate of $1.1 \times 10^{-4} M_\odot$ yr^{-1}. Given its large envelope accretion rate, it is possible that object B is the seed of a high-mass protostar. Observational support for the presence of infalling gas within the central region of the G305.136+0.068 cold core may be found in the observed profiles of the CO(3 → 2) and ^{13}CO(3 → 2) lines, the former one exhibiting a broad asymmetric blueshifted profile and the later a narrower Gaussian profile. Clearly, further observations are needed to investigate this hypothesis. The SED fitting indicates that source A corresponds to a slightly older object (age of 2×10^6 yr), with a mass of 5.8 $M_\odot$, a luminosity of 1.5×10^3 $L_\odot$, without an envelope but with an accretion disk. The SED fitting indicates that source C is not embedded, and that it has an age of 4×10^6 yr, a mass of 3.2 $M_\odot$, a luminosity of 88 $L_\odot$ and that it is associated with a disk that has an outer radius of 80 AU.

5. SUMMARY

We observed molecular line emission in the $J = 3 \rightarrow 2$ transitions of CO and ^{13}CO and in several transitions of CS toward the G305.136+0.068 cold dust core. Also observed was the 0.87 mm continuum emission. The main results and conclusions are summarized as follows.

The molecular core is isolated and roughly circularly symmetric. However, the angular size (FWHM) of the core depends on the transition observed, ranging from 18″ in the CS(7 → 6) transition to 64″ in the CO(3 → 2) transition. This indicates that the core exhibits a steep density dependence with radius. From the CO(3 → 2) and ^{13}CO(3 → 2) observations, we derive an LTE mass of 1.1×10^3 $M_\odot$, in good agreement with the mass derived from the dust observations of 1.2×10^3 $M_\odot$.

The model fit of the CS emission using a Monte Carlo radiative transfer code indicates that the G305.136+0.068 core is very dense and centrally condensed, with a density dependence with radius following a power law with an index of −1.8. The model fit also indicates that the turbulent velocity and temperature increases toward the center of the core following a power law with indices of −0.2 and −0.15, respectively.

A fit to the SED of the emission from millimeter to far-infrared wavelengths gives a dust temperature of 17 K, confirming that the core is cold, and an average column density of 2.6×10^{23} cm^{-2} or equivalently 1.1 g cm^{-2}. This value is slightly above the theoretical threshold value required for the formation of high-mass stars (Krumholz & McKee 2008).

We found two embedded sources within a region of ∼20″ centered at the core. The object closest to the core center

is young, has a luminosity of 66 $L_{\odot}$, and is accreting mass with a high accretion rate, of $\sim 1 \times 10^{-4}\ M_{\odot}\ \mathrm{yr}^{-1}$. This object may correspond to the seed of a high-mass protostar still in the process of formation. All of the above results indicate that G305.136+0.068 corresponds to a massive and dense cold molecular core, in a very early evolutionary stage, in which the formation of a central massive object may have just started.

G.G., Y.C., and D.M gratefully acknowledge support from CONICYT through project BASAL PFB-06. J.E.P. acknowledges funding from the European Community Seventh Framework Programme (/FP7/2007-2013/) under grant agreement No. 229517 and support by the Swiss National Science Foundation, project number CRSII2-141880. A.E.G. acknowledges support from NASA Grants NNX12AI55G and NNX10AD68G. This publication made use of the GLIMPSE-*Spitzer* and Hi-GAL-*Herschel* database.

REFERENCES

Bernes, C. 1979, A&A, 73, 67
Beuther, H., Schilke, P., Menten, K. M., et al. 2002, ApJ, 566, 945
Bourke, T. L., Garay, G., Lehtinen, K. K., et al. 1997, ApJ, 476, 781
Carey, S. J., Noriega-Crespo, A., Mizuno, D. R., et al. 2006, BAAS, 38, 1023
Chini, R., Kruegel, E., & Wargau, W. 1987, A&A, 181, 378
Contreras, Y., Schuller, F., Urquhart, J. S., et al. 2013, A&A, 549, A45
Ezawa, H., Kawabe, R., Kohno, K., & Yamamoto, S. 2004, Proc. SPIE, 5489, 763
Faúndez, S., Bronfman, L., Garay, G., et al. 2004, A&A, 426, 97
Fazio, G. G., Hora, J. L., Allen, L. E., et al. 2004, ApJS, 154, 10
Garay, G., Faúndez, S., Mardones, D., et al. 2004, ApJ, 610, 313
Garay, G., Mardones, D., Brooks, K. J., Videla, L., & Contreras, Y. 2007, ApJ, 666, 309
Garden, R. P., Hayashi, M., Hasegawa, T., Gatley, I., & Kaifu, N. 1991, ApJ, 374, 540
Griffin, M. J., Abergel, A., Abreu, A., et al. 2010, A&A, 518, L3
Hill, T., Burton, M. G., Minier, V., et al. 2005, MNRAS, 363, 405
Juvela, M. 1996, A&AS, 118, 191
Krumholz, M. R., & McKee, C. F. 2008, Natur, 451, 1082
MacLaren, I., Richardson, K. M., & Wolfendale, A. W. 1988, ApJ, 333, 821
Mardones, D. 1998, PhD thesis, Harvard Univ.
Molinari, S., Swinyard, B., Bally, J., et al. 2010, PASP, 122, 314
Mueller, K. E., Shirley, Y. L., Evans, N. J., II, & Jacobson, H. R. 2002, ApJS, 143, 469
Ossenkopf, V., & Henning, T. 1994, A&A, 291, 943
Pineda, J. E., Caselli, P., & Goodman, A. A. 2008, ApJ, 679, 481
Plume, R., Jaffe, D. T., & Evans, N. J., II. 1992, ApJS, 78, 505
Plume, R., Jaffe, D. T., Evans, N. J., II, Martín-Pintado, J., & Gómez-González, J. 1997, ApJ, 476, 730
Poglitsch, A., Waelkens, C., Geis, N., et al. 2010, A&A, 518, L2
Robitaille, T. P., Whitney, B. A., Indebetouw, R., & Wood, K. 2007, ApJS, 169, 328
Schuller, F., Menten, K. M., Contreras, Y., et al. 2009, A&A, 504, 415
Siringo, G., Kreysa, E., Kovács, A., et al. 2009, A&A, 497, 945
Sridharan, T. K., Beuther, H., Saito, M., Wyrowski, F., & Schilke, P. 2005, ApJL, 634, L57
Tafalla, M., Myers, P. C., Caselli, P., & Walmsley, C. M. 2004, A&A, 416, 191
van Zadelhoff, G.-J., Dullemond, C. P., van der Tak, F. F. S., et al. 2002, A&A, 395, 373
Williams, S. J., Fuller, G. A., & Sridharan, T. K. 2004, A&A, 417, 115